



Article

Dynamic Feedforward-Based Fractional Order Impedance Control for Robot Manipulator

Yixiao Ding ¹, Ying Luo ^{1,*} and Yangquan Chen ²

¹ School of Mechanical Science and Engineering, Huazhong University of Science and Technology, Wuhan 430074, China

² Department of Mechanical Engineering, School of Engineering, University of California, Merced, CA 95343, USA

* Correspondence: ying.luo@hust.edu.cn

Abstract: Impedance control is widely applied in contact force control for robot manipulators. The traditional impedance model is linear, and has limitations in describing the actual impedance force. In addition, time-varying and dynamic coupling characteristics pose critical challenges to high-speed and high-precision impedance control. In this paper, a fractional order impedance controller (FOIC) is proposed for industrial robot manipulator control and a systematic FOIC parameters tuning strategy based on frequency-domain specifications is presented. In order to improve performance under dynamic disturbances, a dynamic feedforward-based fractional order impedance controller (DFF-FOIC) is further developed. The robot manipulator dynamics are investigated and the effectiveness of the DFF-FOIC is illustrated by simulation. Then, the DFF-FOIC is applied on a physical robot manipulator prototype. Our step force tracking test results show that the proposed FOIC has better control performance than an integer order impedance controller (IOIC), achieving a better step response with lower overshoot, less settling time, and smaller integral time absolute error (ITAE) than the IOIC under fair comparison conditions.

Keywords: robot manipulator; fractional order impedance control; dynamic feedforward control



Citation: Ding, Y.; Luo, Y.; Chen, Y. Dynamic Feedforward-Based Fractional Order Impedance Control for Robot Manipulator. *Fractal Fract.* **2023**, *7*, 52. <https://doi.org/10.3390/fractalfract7010052>

Academic Editor: Norbert Herencsar

Received: 10 September 2022

Revised: 19 December 2022

Accepted: 22 December 2022

Published: 1 January 2023



Copyright: © 2023 by the authors. Licensee MDPI, Basel, Switzerland. This article is an open access article distributed under the terms and conditions of the Creative Commons Attribution (CC BY) license (<https://creativecommons.org/licenses/by/4.0/>).

1. Introduction

Robotic manipulators are widely applied in various fields, including assembly lines [1], spray lacquering [2], and palletizing [3]. In modern manufacturing and human interaction scenes, it is desirable to control the contact force between the robot end and the environment. For example, in the grinding process for complex robotic geometries, the surface machining consistency is hard to guarantee with only trajectory planning control [4]. In robot-assisted needle insertion, the lack of force feedback and control increases tissue deformation and reduces surgeons' controllability of surgical instruments [5]. Single-position control cannot meet the force perception requirements of these working scenes.

Robot manipulator contact force control has been extensively studied in academic communities and for industrial applications [6]. Position-based impedance control is a common method for robot manipulators [7], based on an outer force control loop and inner position control loop [8]. The traditional mass-spring-damper impedance model is linear, as described in [9]; the integer order model cannot model the impedance force of the physical environment precisely, and the parameter tuning of the impedance controller is limited [10,11]. The fractional order model, with its characteristics of heredity, memory, and nonlinearity, can describe the physical system more accurately [12,13], and is widely used in system modeling and controller design [14,15]. Damping force modeling in viscoelastic dampers was studied in [16]; the results showed that the fractional order derivative-based damper model was more accurate and required fewer parameters compared to the integer model. In [17], a fractional order damping force model based on the fractional Euler–Lagrange equation was proposed to describe the damped oscillating system, and showed

better performance than the integer order model. In this paper, a fractional order impedance controller (FOIC) is proposed using a fractional order theory-based damping force model. The fractional order impedance model can describe the contact force more precisely, and FOIC has more tuning parameters and better control performance than IOIC. In addition, a systematic parameter design strategy for FOIC is proposed for optimal controller tuning based on frequency-domain specifications.

In order to further improve the FOIC control performance with high dynamic response requirement, a dynamic feedforward-based fractional order impedance controller (DFF-FOIC) for robot manipulators is proposed. High performance motion is the foundation of machining quality and working efficiency for robot manipulators, and requires high dynamic response and high robustness for controllers [2]. However, robot manipulator dynamics feature high nonlinearity and strong coupling, and are time-variant [18]. The dynamic characteristics have non-negligible effects on motion accuracy, especially in high-magnitude and high-speed motion scenes [19]. Large inertia changes degrade high-speed response, and can lead to system oscillation. In addition, the motion accuracy is affected by system friction [20]. Low machining accuracy and poor lubrication conditions increase the friction significantly [2]. In high speed working scenes, friction seriously affects the desired robot dynamic response and robustness performance [21]. Conventional closed-loop controllers are mainly aimed at the linear constant system; conservative control parameters limit the system gain bandwidth and affect the system's dynamic response performance [22]. A model-based controller has the ability to reduce nonlinearity for better control performance [23], with a dynamic model feedforward-based controller being an effective method for a robot system to achieve the desired dynamic response and high robustness performance [24]. The DFF-FOIC for robot manipulators proposed in this paper can improve the transient response performance. Accurate dynamic parameters are the foundation of the DFF-FOIC. Dynamic model parameters can be obtained by precise identification methods [25]. In this paper, the Newton–Euler method is used to establish the robot dynamic model [26]. The finite Fourier series is applied as the excitation trajectory to excite the dynamic characteristic for the robot manipulator [27]. The least squares estimator method is used to obtain the identified dynamic parameters [28].

The main contributions of this paper are as follows: (1) A dynamic feedforward-based fractional order impedance controller (DFF-FOIC) for robot manipulators is proposed with optimized impedance modeling accuracy to reduce the impact of robot dynamics with disturbance due to the non-negligible effects of highly nonlinear features, strong coupling, and time variance. (2) The effectiveness of the proposed DFF-FOIC is illustrated in simulation and validated using an industrial robot manipulator experimental platform. The results show that FOIC has better performance than IOIC under the same design specifications. DFF-FOIC can improve the dynamic response and guarantee high robustness performance compared with existing methods.

The rest of this paper is organized as follows: in Section 2, the design of the FOIC and dynamic robot manipulator model are proposed; Section 3 demonstrates the simulation analysis of FOIC and DFF-FOIC and the experimental verification is realized; Section 4 concludes the article.

2. Control Design

2.1. Fractional Calculus and Definitions

The fractional order model is the generalization of the traditional integer order model. The fractional calculus of function $f(t)$ is defined as

$${}_a D_t^\alpha f(t) = \begin{cases} \frac{d^\alpha}{dt^\alpha} f(t), & \operatorname{Re}(\alpha) > 0 \\ f(t), & \operatorname{Re}(\alpha) = 0 \\ \int_a^t f(\tau) (d\tau)^{-\alpha}, & \operatorname{Re}(\alpha) < 0, \end{cases} \quad (1)$$

where ${}_aD_t^\alpha$ is the basic operator of fractional calculus, α is the operator order, a and t are the limits of the fractional order operator, and $Re(\alpha)$ represents the real part of α .

Caputo’s definition is one of the most commonly used definitions of fractional derivatives [29]:

$${}_0D_t^\alpha f(t) = \frac{1}{\Gamma(1-\gamma)} \int_0^t \frac{f^{(m+1)}(\tau)}{(t-\tau)^\gamma} d\tau, \tag{2}$$

where $\alpha = m + \gamma$, m is an integer, and $0 < \gamma \leq 1$.

2.2. Design of FOIC

The impedance model consists of a mass, spring, and damper, which dynamically adjust the robot’s posture according to the contact force. The impedance model is shown in Figure 1.

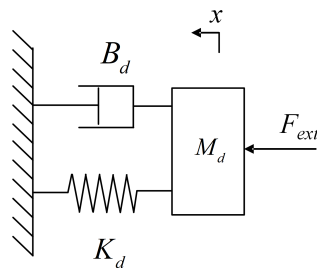


Figure 1. Impedance dynamics model.

The impedance dynamics equation is

$$M_d \ddot{x}(t) + B_d \dot{x}(t) + K_d x(t) = F_{ext}, \tag{3}$$

where M_d is the mass coefficient, B_d is the damper coefficient, K_d is the spring coefficient, F_{ext} is the external force applied to the system, x is the position, and t is the time. The kinematics parameters and external force are dynamically adjusted according to the desired impedance model.

Fractional order theory can be applied to describe the impedance model more accurately than the typical integer order model. In this paper, a fractional order impedance model is proposed with a fractional order damping force model. Thus, Equation (3) can be rewritten as

$$M_d \ddot{x}(t) + B_d D_t^u x(t) + K_d x(t) = F_{ext}, \tag{4}$$

where D_t^u is the fractional order derivative operator and $u \in (0, 2)$ is the operator order.

The FOIC structure is shown in Figure 2, where $B_d s^u$ is the fractional order damping force model, F_{ref} is the reference contact force, F_{real} is the real force obtained from the force sensor, and ΔF is the error between F_{ref} and F_{real} ; moreover, ΔX is the desired position adjustment value, X_0 is the original position of robot manipulator end, X_{cmd} is the final position command, and K_s is the spring coefficient of the environment. Due to the high control bandwidth and high control performance of robot manipulator servo systems, the robot position closed loop is represented as 1 to simplify the control system.

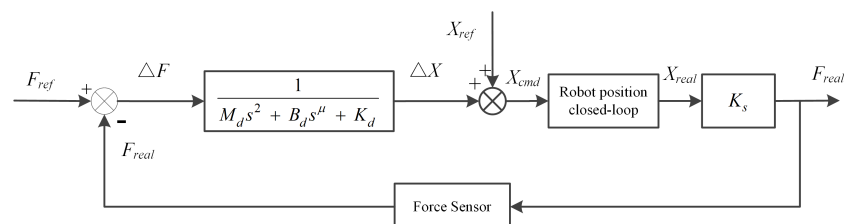


Figure 2. Robot manipulator FOIC control system diagram.

The open-loop transfer function is expressed as

$$G_o(s) = \frac{K_s}{M_d s^2 + B_d s^u + K_d}. \quad (5)$$

The closed-loop transfer function is

$$\Phi(s) = \frac{K_s}{M_d s^2 + B_d s^u + K_d + K_s}. \quad (6)$$

In a position-based impedance controller, the virtual spring can lead to a steady-state force tracking error [8,30]. Many strategies have been presented to deal with this problem [31,32]. Setting the virtual spring stiffness to 0 is a simple way to eliminate the tracking error [30], and is the approach used in this paper. Setting K_d to 0, we have

$$G_o(s) = \frac{K_s}{M_d s^2 + B_d s^u}. \quad (7)$$

Substituting $j\omega$ for s in Equation (7), we have

$$G_o(j\omega) = \frac{K_s}{M_d (j\omega)^2 + B_d (j\omega)^u}. \quad (8)$$

An effective controller parameter tuning method is essential for FOIC. Manual tuning is a common method in impedance controller design. As a trial and error strategy, manual tuning is complicated and difficult to implement in different working scenes [33]. Optimization algorithms are another typical method used in designing impedance controllers, although this approach is often time-consuming and unstable [34]. In order to improve the usability of FOIC, a systematic method for tuning parameters based on the frequency domain is proposed. The proposed strategy for tuning the FOIC parameters based on the frequency domain is an analytical method. In this way, the stability of the designed controller can be guaranteed, rather than using test verification as in [34]. In addition, the analytical method is easy to calculate and implement in the robot control system, and does not require a high-performance computer or time-consuming optimization process. The frequency-domain specifications reflect the controller's fundamental performance, and are easy for engineers to use in different working scenes.

The proposed FOIC tuning method is presented below. Two frequency-domain specifications and one time-domain specification are used, including the gain crossover ω_c , phase margin φ_m , and integral time square error (ITSE).

(1) Gain crossover

$$|G_o(j\omega_c)|_{db} = 1. \quad (9)$$

(2) Phase margin

$$\text{Arg}[G_o(j\omega_c)] = -\pi + \varphi_m. \quad (10)$$

The gain and phase of $G_o(s)$ are as follows:

$$|G_o(j\omega)|_{db} = \frac{K_s}{\sqrt{[M_d(j\omega)^2 + (B_d p_1)]^2 + (B_d p_2)^2}}, \quad (11)$$

$$\varphi(\omega) = -\arctan \frac{B_d p_2}{M_d(j\omega)^2 + B_d p_1}. \quad (12)$$

where

$$p_1 = \omega^u \cos\left(\frac{\pi}{2}u\right),$$

$$p_2 = \omega^u \sin\left(\frac{\pi}{2}u\right).$$

Substituting the given gain crossover ω_c and the desired phase margin φ_m into Equations (9) and (10), we have

$$M_d = \frac{K_s}{a}, \quad (13)$$

$$B_d = bM_d. \quad (14)$$

where

$$a = \sqrt{[(j\omega_c)^2 + bp_1]^2 + (bp_2)^2},$$

$$b = \frac{(j\omega_c)^2 \tan(\pi - \varphi_m)}{p_2 - p_1 \tan(\pi - \varphi_m)}.$$

Another time-domain specification ITSE is used to design the FOIC, as follows,

$$J_{ITSE} = \int_0^{t_f} t[e(t)]^2 dt, \quad (15)$$

where t_f is the final time and $e(t)$ is the error between the reference and the actual value corresponding to time t .

The systematic FOIC parameters tuning strategy can be summarized with the following example:

- (1) With a gain crossover $\omega_c = 30$ rad/s, phase margin $\varphi_m = 40^\circ$, $F_{ref} = 20$ N, and $K_s = 1293.83$ N/m, the real spring stiffness can be identified.
- (2) By sweeping $u \in (0, 2)$, all the controllers satisfying ω_c and φ_m are calculated according to Equations (13) and (14).
- (3) In this step, we implement the step response simulation or the contact force disturbance simulation in steady state of the FOIC considering the desired performance. If tracking performance is mainly being considered, we implement the step response simulation of the FOIC obtained above in (2), then calculate the corresponding J_{ITSE} . If the anti-disturbance performance is mainly being considered, we implement the contact force disturbance simulation of all the FOIC obtained above in (2) in steady state, then calculate the corresponding J_{ITSE} . In the example used here, the tracking performance is mainly being considered, and the step response simulation is implemented.
- (4) The FOIC according to the smallest J_{ITSE} is selected as the final controller, with $M_d = 1.0722$ kg, $B_d = 25.9117$ N·s/m, and $u = 1.02$.

The effects of the control parameters on the performance of the closed-loop system are discussed below. By sweeping $u \in (0, 2)$, all the controllers satisfying $\omega_c = 30$ rad/s for a phase margin $\varphi_m = 40^\circ$ are shown in Figure 3. The performance of FOIC with different control parameters are compared by ITSE. The correspondence diagram between ITSE and u is shown in Figure 4. The red dot in Figures 3 and 4 is the FOIC designed above.

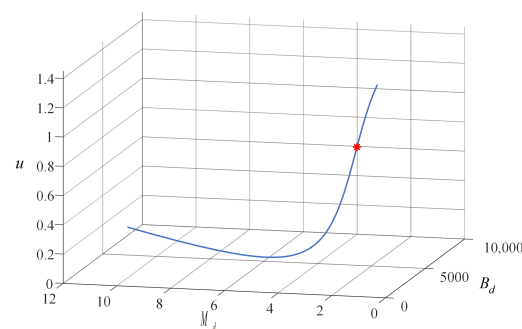


Figure 3. All FOIC satisfying the given ω_c and φ_m .

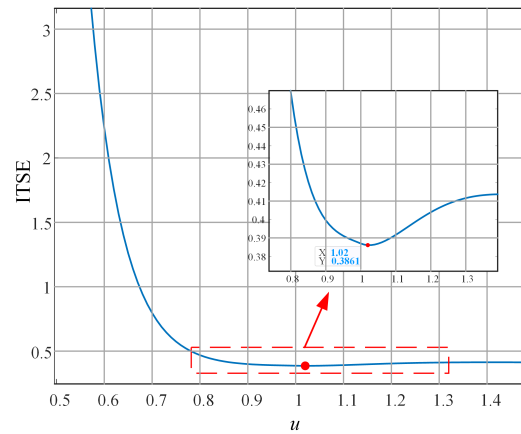


Figure 4. J_{ITSE} of FOIC corresponding to u .

2.3. Stability Analysis

In this subsection, a stability analysis of the FOIC closed-loop system is conducted.

Lemma 1. An ordinary input/output relation (with only integer derivatives) can be written in a polynomial representation:

$$\begin{aligned} P(\sigma)\xi &= Q(\sigma)u, \\ y &= R(\sigma)\xi, \end{aligned} \tag{16}$$

where $u \in \mathfrak{R}^{\bar{m}}$ is the control, $\xi \in \mathfrak{R}^{\bar{n}}$ is the partial state, and $y \in \mathfrak{R}^{\bar{p}}$ is the output; here, P , Q and R are polynomial matrices in the variable σ of dimensions $\bar{n} \times \bar{n}$, $\bar{n} \times \bar{m}$, and $\bar{p} \times \bar{n}$, respectively, and σ can be seen as the symbol of the usual derivative s^α when all initial conditions are zero.

For a proof of Lemma 1, see [35].

If the triplet (P, Q, R) of polynomial matrices is minimal, we have the following equivalence: System (16) is bounded-input bounded-output iff $\det(P(\sigma)) \neq 0 \forall \sigma, |\arg(\sigma)| < \alpha\pi/2$.

Theorem 1. When choosing appropriate FOIC parameters (M_d, B_d , and u) to ensure that

$$|\arg(w_i)| > \lambda \frac{\pi}{2}, \tag{17}$$

where w_i represents the i th root of the equation

$$M_d w^{2q} + B_d w^p + K_s = 0, \tag{18}$$

where $\lambda = 1/q$, $p/q = u$, p , and q are positive integers, then the closed-loop system is bounded, as $t \rightarrow \infty$.

Proof. The structure of FOIC for a robot manipulator is as shown in Figure 2. Due to the high control bandwidth and high control performance of robot manipulator servo systems, the robot’s closed-loop position is represented as 1 to simplify the control system. The transfer function of the force sensor is 1 due to its high performance.

The closed-loop transfer function of FOIC with $K_d = 0$ is

$$\Phi(s) = \frac{K_s}{M_d s^2 + B_d s^u + K_s}. \tag{19}$$

The characteristic equation of Equation (19) is

$$N(s) = M_d s^2 + B_d s^u + K_s. \tag{20}$$

We note that

$$u = \frac{p}{q}, s^u = s^{p/q}, \quad (21)$$

where p and q are positive integers.

Thus,

$$N(s) = M_d s^2 + B_d s^{p/q} + K_s, \quad (22)$$

We denote $\lambda = 1/q$, $w = s^\lambda$; then,

$$N(w) = M_d w^{2q} + B_d w^p + K_s = 0. \quad (23)$$

According to Lemma 1, $\tilde{m} = 1$, $\tilde{n} = 1$, and

$$|\arg(w_i)| > \lambda \frac{\pi}{2}, \quad (24)$$

therefore, the closed-loop system is bound-input bound-output. \square

With the help of Theorem 1, we can state the FOIC considering the robot manipulator system rather than using a gain of 1.

Theorem 2. When choosing proper FOIC parameters M_d , B_d , and u to ensure that

$$|\arg(w_i)| > \lambda \frac{\pi}{2}, \quad (25)$$

where w_i represents the i th root of the equation

$$M_d b_2 s^4 + B_d b_2 s^{u+2} + M_d b_1 s^3 + B_d b_1 s^{u+1} + M_d b_0 s^2 + B_d b_0 s^u + K_s a_1 s + K_s a_0 = 0, \quad (26)$$

where $\lambda = 1/q$, $p/q = u$, p , and q are positive integers, M_d , B_d , are the parameters of FOIC, and a_0 , a_1 , b_0 , b_1 , and b_2 are the parameters of the robot manipulator system, then the closed-loop system is bounded, as $t \rightarrow \infty$.

Proof. The structure of the FOIC for robot manipulator is as shown in Figure 2. The closed-loop transfer function of the FOIC with $K_d = 0$ is

$$\Phi_2(s) = \frac{(a_1 s + a_0) K_s}{M_d b_2 s^4 + B_d b_2 s^{u+2} + M_d b_1 s^3 + B_d b_1 s^{u+1} + M_d b_0 s^2 + B_d b_0 s^u + K_s a_1 s + K_s a_0}. \quad (27)$$

The characteristic equation of Equation (27) is

$$N_2(s) = M_d b_2 s^4 + B_d b_2 s^{u+2} + M_d b_1 s^3 + B_d b_1 s^{u+1} + M_d b_0 s^2 + B_d b_0 s^u + K_s a_1 s + K_s a_0. \quad (28)$$

We note that

$$u = \frac{p}{q}, s^u = s^{p/q}, \quad (29)$$

where p and q are positive integers.

Thus,

$$N_2(s) = M_d b_2 s^4 + B_d b_2 s^{2+p/q} + M_d b_1 s^3 + B_d b_1 s^{1+p/q} + M_d b_0 s^2 + B_d b_0 s^{p/q} + K_s a_1 s + K_s a_0. \quad (30)$$

We denote $\lambda = 1/q$, $w = s^\lambda$; then,

$$N_2(w) = M_d b_2 w^{4q} + B_d b_2 w^{2q+p} + M_d b_1 w^{3q} + B_d b_1 w^{q+p} + M_d b_0 w^{2q} + B_d b_0 w^p + K_s a_1 w^q + K_s a_0 = 0. \quad (31)$$

According to Lemma 1, $\tilde{m} = 1$, $\tilde{n} = 1$, and

$$|\arg(w_i)| > \lambda \frac{\pi}{2}, \quad (32)$$

therefore, the closed-loop system is bound-input bound-output. \square

2.4. Dynamic Model for Robot Manipulator

The disturbance dynamics of robotic manipulators has the characteristics of time variance, high nonlinearity, and strong coupling. These disturbances pose a challenge for the control performance of FOIC with dynamic response and robustness requirements. Dynamic feedforward, as a model-based control strategy, can effectively and fundamentally reduce the influence of robot disturbance dynamics.

The dynamic model for a robot manipulator is as follows:

$$\tau = H(q)\ddot{q} + C(q, \dot{q})\dot{q} + G(q) + F(\dot{q}), \quad (33)$$

where q , \dot{q} , and \ddot{q} are the vector of joint positions, velocities, and accelerations, respectively, H is the inertia matrix, C is the Coriolis and centripetal coupling matrix, G is the gravity load, F is the friction force, and τ is the vector of actuator forces driving the links. In this paper, the Coulomb viscous friction model is used, as follows:

$$F = T_c + B_m\dot{q}, \quad (34)$$

$$T_c = \begin{cases} T_c^+, & \dot{q} > 0 \\ 0, & \dot{q} = 0 \\ T_c^-, & \dot{q} < 0, \end{cases} \quad (35)$$

where T_c and B_m are the Coulomb friction and viscous friction coefficients, respectively, and T_c^+ and T_c^- are the different Coulomb friction coefficients corresponding to the rotation of the velocity \dot{q} .

Here, τ is linearly related to the dynamic parameters, and Equation (33) can be rewritten as follows [36]:

$$\tau = Y(q, \dot{q}, \ddot{q})P, \quad (36)$$

where $P = [P_1, P_2, \dots, P_j]$ (with j being the number of links) is the vector of the dynamic parameters; for link i , $P_i = [xx_i, xy_i, xz_i, yy_i, yz_i, zz_i, mx_i, my_i, mz_i, m_i, T_{ci}^+, T_{ci}^-, B_{mi}, J_{mi}]$, where $xx_i, xy_i, xz_i, yy_i, yz_i, zz_i$ are the moments of inertia, mx_i, my_i, mz_i are the first moment, m_i is the link mass, T_{ci}^+ and T_{ci}^- are the Coulomb friction coefficients, B_{mi} is the viscous friction coefficient, J_{mi} is the motor inertia, and $Y(q, \dot{q}, \ddot{q})$ is the regressor matrix according to P .

The robot manipulator's dynamic parameters need to be identified. A standard robot identification process includes model establishment, data acquisition, and data estimation [25]. The dynamics model is linear to P ; however, not all of the parameters have effects on the motion [22], which means that Y is not full rank. In order to identify the dynamic parameters, the base parameters-based dynamics model is used for the identification [26]. As for data acquisition, the finite Fourier series excitation trajectories are used to excite the robot dynamics; this approach has the advantages of time-domain data averaging and a specifiable bandwidth of the excitation trajectories [27]. In addition, the velocities and accelerations can be obtained according to the approximated sine and cosine functions of the measured joint position information. Finally, the dynamic parameters are identified as follows:

$$P' = (Y'^T Y')^{-1} Y'^T \tau, \quad (37)$$

where P' represents the base parameters, Y' is the regressor matrix to P' , Y'^T is the transpose of Y' , and τ is the driving force vector of the actuators.

An identification process for the EFORT ERC20C-C10 industrial robot manipulator is presented below.

As mentioned above, the finite Fourier series excitation trajectories are applied for identification, as follows [27]:

$$q_i = \sum_{l=1}^5 \left[\frac{a_{l,i}}{\omega_f l} \sin(\omega_f l t) - \frac{b_{l,i}}{\omega_f l t} \cos(\omega_f l t) \right] + q_{i0}, \quad (38)$$

where q_i is the trajectory of $joint_i$ ($i = 1, 2, 3$), the base frequency $\omega_f = 0.2\pi$, $q_{10} = 0.1093$, $q_{20} = -0.1310$, $q_{30} = 0.0430$, the coefficients $a_{l,i}$ and $b_{l,i}$ are listed in Table 1, and the trajectories are shown in Figure 5.

Table 1. The coefficients of the Fourier series excitation trajectory.

i	$a_{1,i}$	$a_{2,i}$	$a_{3,i}$	$a_{4,i}$	$a_{5,i}$
1	-0.0768	-0.0675	-0.0457	0.0521	0.1379
2	-0.1505	-0.0172	-0.1307	0.2954	0.0030
3	-0.0576	0.0177	0.0479	-0.6920	0.6840
i	$b_{1,i}$	$b_{2,i}$	$b_{3,i}$	$b_{4,i}$	$b_{5,i}$
1	-0.0571	0.2280	-0.0809	0.4996	-0.4309
2	-0.1795	0.2032	-0.0809	0.2786	0.0938
3	0.0019	0.2032	-0.0809	0.1852	0.1510

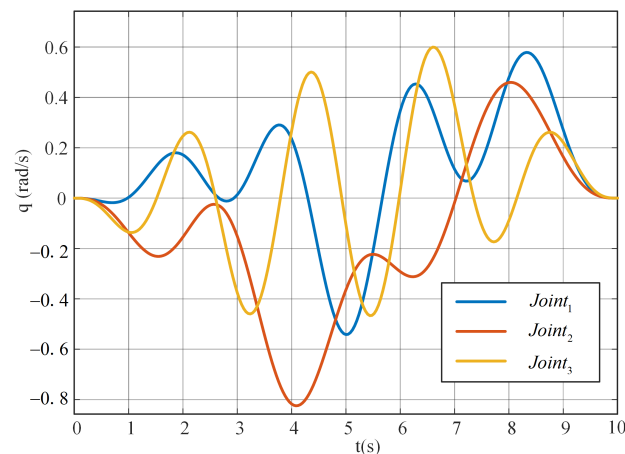


Figure 5. The Fourier series excitation trajectory.

The identified base dynamic parameters of the EFORT ERC20C-C10 are shown in Table 2. The measured and the calculated joint driving torque based on the identified base dynamic parameters of the excitation trajectory are shown in Figure 6. The root mean square errors (RMSE) of the three joints are 0.4223 Nm, 0.3730 Nm, and 0.3162 Nm, respectively, which verifies that the identified dynamic parameters are accurate.

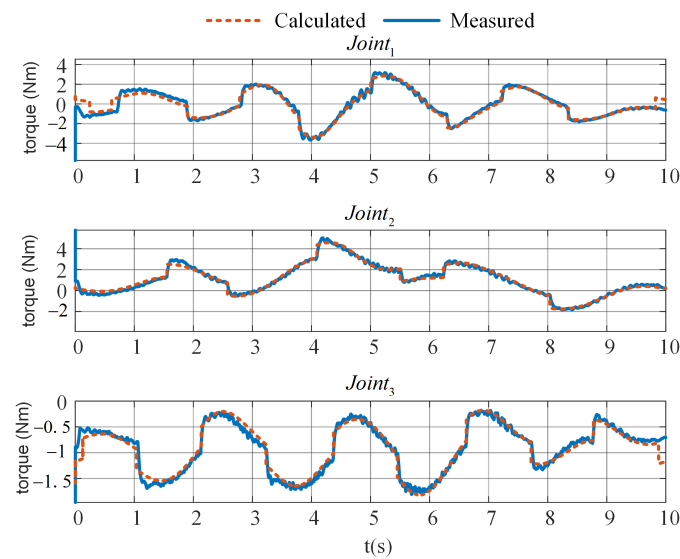


Figure 6. Measured and calculated joint-driving torque values.

Table 2. Base dynamic parameters of the ERC20-C10.

Item	zz_1 (Kgm ²)	xx_2 (Kgm ²)	xy_2 (Kgm ²)	xz_2 (Kgm ²)	yz_2 (Kgm ²)
Value	27.88541	116.4740	−11.9243	8.63456	−13.4807
Item	zz_2 (Kgm ²)	mx_2 (Kgm)	my_2 (Kgm)	xx_3 (Kgm ²)	xy_3 (Kgm ²)
Value	70.4156	−10.1249	48.6138	27.8231	−2.0144
Item	xz_3 (Kgm ²)	yz_3 (Kgm ²)	zz_3 (Kgm ²)	mx_3 (Kgm)	my_3 (Kgm)
Value	−7.4829	20.6031	−3.6640	17.5760	4.0855
Item	J_3 (m ²)	T_{c1}^+ (Nm)	T_{c1}^- (Nm)	B_{m1} (Nms/rad)	T_{c2}^+ (Nm)
Value	12.9752	62.00688	−93.8778	116.3661	176.8584
Item	T_{c2}^- (Nm)	B_{m2} (Nms/rad)	T_{c3}^+ (Nm)	T_{c3}^- (Nm)	B_{m3} (Nms/rad)
Value	−38.5557	119.6391	17.64926	−47.8277	89.00266

$xx_i, xy_i, xz_i, yy_i, yz_i, zz_i$ are the moments of inertia of link i about the center of its frame, mx_i, my_i, mz_i are the first moment of link i , m_i is the mass of link i , T_{ci}^+ and T_{ci}^- are the Coulomb friction coefficients of $joint_i$, B_{mi} is the viscous friction coefficient of $joint_i$, J_i is the motor inertia (output shaft referred) of $joint_i$.

3. Simulation and Experimental Results

3.1. Simulation Illustration

3.1.1. Simulation System

In this section, the construction of an FOIC simulation system for a six degrees of freedom (6DoF) robot manipulator is described. A robot kinematic block and servo block with dynamic disturbance and dynamic feedforward block are designed considering the influence of the robot system and disturbance dynamics, as shown in Figure 7 and Table 3.

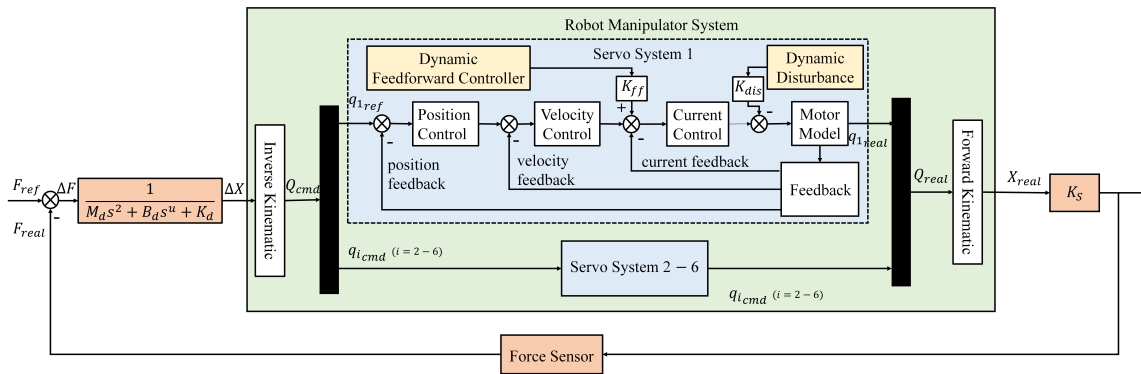


Figure 7. Robot manipulator FOIC simulation system.

Table 3. Simulation system components and function.

Component		Function	
Robot System	FOIC	Adjust the dynamic relation between the contact force error and robot end position	
	Inverse Kinematic	Calculate the joint position command Q_{cmd} , a six-dimension vector consisting of all the joint command of the 6-Axis robot manipulator, according to the robot end command in cartesian coordinate	
	Servo System	Control Loop	Consist of position-control-loop, velocity-control-loop and current-control-loop
		Motor Model	A motor model with friction and inertia
		Dynamic Disturbance	The inverse dynamic results are used as the dynamic disturbance for the servo system, to simulate the influence of inertia, gravity and friction in the real physical environment
		Dynamic Feedforward Controller	Calculate the driving torque corresponding to the desired kinematic command Q_{cmd} according to Equation (36). Transform the driving torque to driving current by K_{ff} and compensate the dynamic disturbance
		K_{dis}	Conversion coefficient between disturbance torque and current
		K_{ff}	Conversion coefficient between dynamic feedforward torque and current
	Forward Kinematic	Calculate the position of the robot end in cartesian coordinate according to the joint real position Q_{real} , a six-dimension vector consisting of real position of every joint of the 6-Axis robot manipulator	
	K_s	Simulate the external spring stiffness contacting with the end of robot	
Force Sensor	Obtain the real contact force		

The Puma560 6DoF robot manipulator is applied as the robot in simulation. The modified Denavit–Hartenberg (DH) parameters are shown in Table 4. In the impedance test, $Joint_4$, $Joint_5$, and $Joint_6$ are without motion; thus, the dynamic parameters of the above joints are all neglected as 0. The dynamic parameters of the Puma560 are listed in Table 5. Considering the reference trajectory and dynamic parameters, we can obtain the required

actuator driving forces τ according to Equation (36), which can be used as the dynamic disturbance.

Table 4. Puma560 modified Denavit–Hartenberg (DH) parameters.

Link	Joint Offset (d) (m)	Link Length (a) (m)	Link Twist (α) (rad)
1	0	0	1.5708
2	0	0.4318	0
3	0.15005	0.0203	−1.5708
4	0.4318	0	1.5708
5	0	0	−1.5708
6	0	0	0

Table 5. Puma560 dynamic parameters.

	xx (Kgm ²)	xy (Kgm ²)	xz (Kgm ²)	yy (Kgm ²)	yz (Kgm ²)
$link_1$	0	0	0	0	0
$link_2$	0.13	0	0	0.524	0
$link_3$	0.066	0	0	0.0125	0
	zz (Kgm ²)	mx (Kgm)	my (Kgm)	mz (Kgm)	m (Kg)
$link_1$	0.35	0	0	0	0
$link_2$	0.539	1.1832	0.1044	−0.2784	17.4
$link_3$	0.066	0	−0.336	0.0672	4.8
	T_c^+ (Nm)	T_c^- (Nm)	B_m (Nms/rad)	G	J_m (Kg m ²)
$joint_1$	0.395	−0.435	0.00148	−62.61	0.000291
$joint_2$	0.126	−0.071	0.000817	107.8	0.000409
$joint_3$	0.132	−0.105	0.00138	−53.71	0.00299

xx, xy, xz, yy, yz, zz are the moments of inertia about the center of gravity (COG), mx, my, mz are the first moment, m is the link mass, T_c^+ and T_c^- are the Coulomb friction coefficients, B_m is the viscous friction coefficient, G is the gear ratio, J_m is the motor inertia (motor referred).

3.1.2. Fractional Order Operator Implementation

The FOIC designed in Section 2 was tested via simulation. The fractional order $\frac{1}{s^u}$ is realized by the impulse response-invariant discretization method [37]. The approximate transfer function order is set as 7 and the sampling frequency is set as 1 KHz. The discretized transfer function of $\frac{1}{s^{1.02}}$ is written as

$$\frac{1}{s^u} = \frac{1}{s^{1.02}} = \frac{B(z^{-1})}{A(z^{-1})}, \quad (39)$$

where:

$$B(z^{-1}) = 0.8686z^7 - 3.592z^6 + 5.997z^5 - 5.146z^4 + 2.385z^3 - 0.5696z^2 + 0.05899z - 0.001574 \text{ and } A(z^{-1}) = z^7 - 4.156z^6 + 6.978z^5 - 6.03z^4 + 2.82z^3 - 0.6817z^2 + 0.07194z - 0.001998.$$

A comparison of the approximated Bode diagram and true Bode diagram is shown in Figure 8. The discretized open-loop Bode plot of the designed FOIC is shown in Figure 9. It can be seen the control system satisfies the given crossover frequency and phase margin specifications.

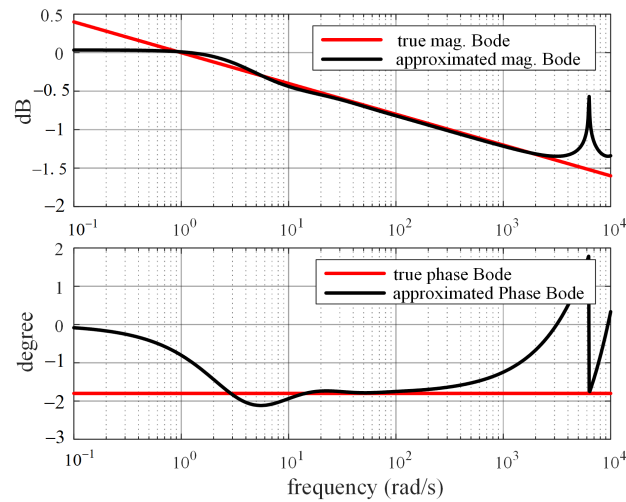


Figure 8. Comparison of approximated Bode diagram and true Bode diagram.

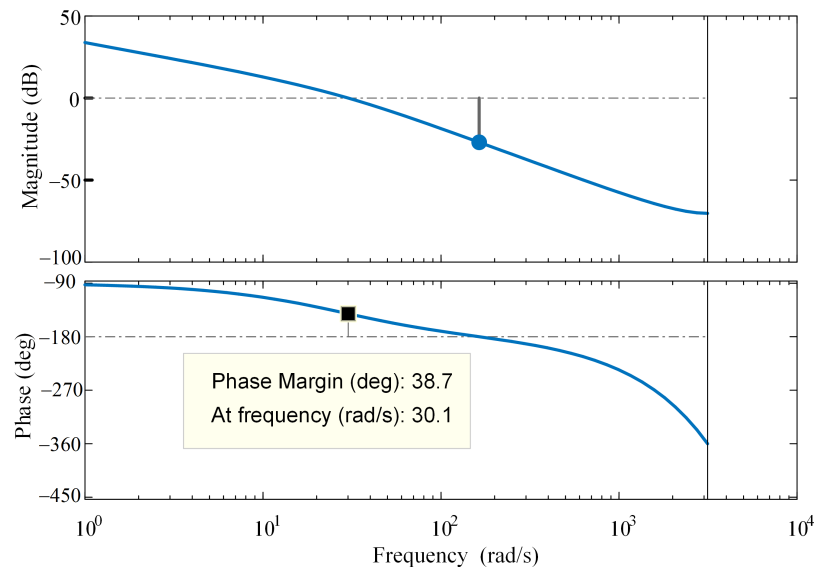


Figure 9. Open-loop Bode diagram of FOIC.

3.1.3. Step Response Simulation

In this section, the contact force step response simulation for FOIC designed above in Section 2.2 ($\omega_c = 30$ rad/s, $\varphi_m = 40^\circ$) is carried out with $M_d = 1.0722$ kg, $B_d = 25.9117$ N·s/m, and $u = 1.02$.

The influence of dynamic disturbance is studied and the effectiveness of the dynamic feedforward method is verified. The dynamic characteristics of $Joint_2$ and $Joint_3$ are considered in this part, which are the main motion joints in the simulation. Setting the reference force as 20 N, the following tests are investigated:

(1) Link inertia and gravity

In order to study the influence of link inertia and gravity disturbance, three different disturbance coefficients ($K_{dis} = 0$, $K_{dis} = 20$, and $K_{dis} = 50$) in the FOIC were tested. The step response simulation results are shown in Figure 10. As can be seen, link inertia and gravity disturbance increase the overshoot, meaning that the system needs more time to reach steady state.

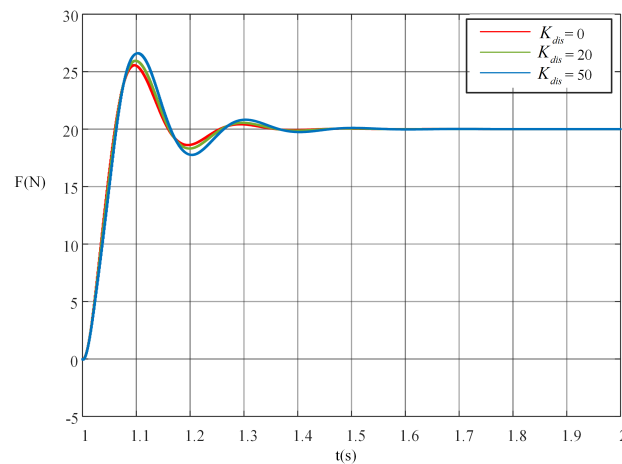


Figure 10. Force step response of the FOIC with dynamic inertia and gravity disturbance changes.

(2) Friction

Coulomb Friction disturbance is considered in this part. In order to better investigate the effectiveness of the friction disturbance, the disturbance coefficient is set as $K_{dis} = 20$, as above, and the Coulomb friction coefficient T_c of $Joint_2$ and $Joint_3$ is adjusted. Here, K_f is used as the amplification coefficient for T_c . In this way, the influence of friction disturbance is investigated alone without any impact from changing the link inertia and gravity. The response curves of the contact force with three different T_c amplification coefficients, $K_f = 1$, $K_f = 2$, and $K_f = 3$, are shown in Figure 11. The results clearly indicate that Coulomb friction disturbance can induce contact force variations. When friction is stronger, the contact force fluctuation is larger.

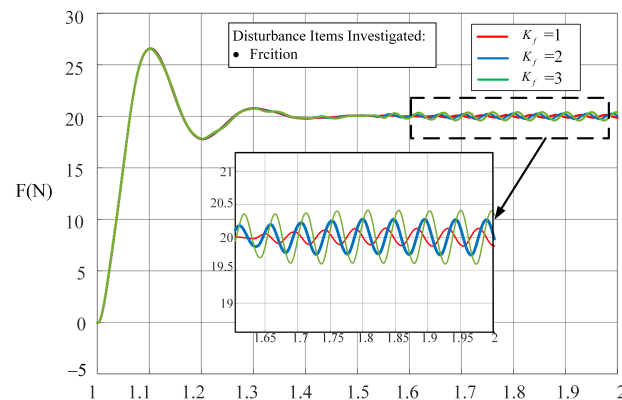


Figure 11. The force step responses of FOIC with friction disturbance.

(3) Link inertia, gravity, and friction.

For further validation, all the dynamic impact factors, that is, link inertia, gravity, and friction, were taken into account together. The friction parameters in Table 5 were used. The force tracking performances were compared under three different disturbance coefficients $K_{dis} = 0$, $K_{dis} = 20$, $K_{dis} = 50$. The response curves of the system output are presented in Figure 12. The results show the combined characteristics of the previous two items. As the growth in the disturbance coefficient increases, the system has a worse response speed, larger overshoot, longer settling time, and larger force fluctuation.

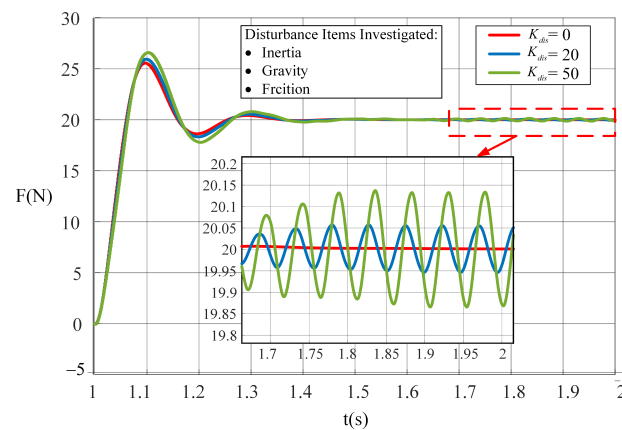


Figure 12. Force step response of the FOIC with inertia, gravity, and friction disturbances.

To verify the effectiveness of the dynamic feedforward method, the dynamic parameters in Table 5 were used. Dynamic disturbance with coefficient $K_{dis} = 20$ was applied for the test. Three different levels of compensation simulation with feedforward coefficients of $K_{ff} = 0$, $K_{ff} = 2.5$, and $K_{ff} = 5$ are presented in Figure 13. The results show that dynamic feedforward can effectively suppress the dynamic disturbance. The controller with dynamic feedforward achieves a better response speed, can suppress the overshoot caused by dynamic disturbance, and has a shorter settling time and better robustness performance compared with the controller without dynamic feedforward.

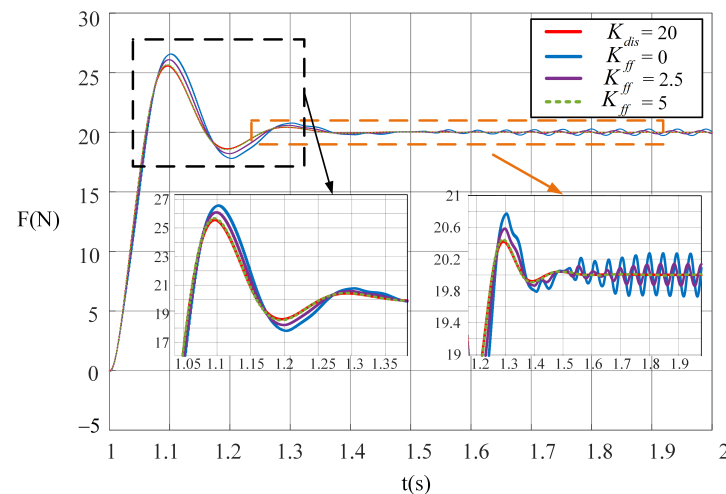


Figure 13. Force step response of the DFF-FOIC with dynamic disturbances.

3.2. Experimental Verification

3.2.1. Experimental Setup

This section describes the experiments we carried out. The experimental setup consisted of a 6DoF EFORT ER20C-C10 industrial robot manipulator, an ADVANTECH industrial computer with a self-developed robot controller and self-developed human–computer interface software, a 6DoF HPS-FT060E force sensor, and a spring, as shown in Figure 14. Communication between the equipment used EtherCAT. An Igh-EtherCAT master stack was embedded in the self-developed robot controller to communicate with other EtherCAT slaves, including the servo system and the force sensor. The communication update frequency was set as 1 KHz. The detailed experimental setup information is shown in Table 6. The modified DH parameters for robot manipulator are listed in Table 7. The identified base dynamic parameters are shown in Table 2. In TSINO DYNATRON CoolDrive R6, the object dictionary data index 60B2_l of EtherCAT, described as the torque offset, is used as the

dynamic feedforward torque transmission interface from the Igh-EtherCAT master stack in the self-developed controller to the EtherCAT slaves. The torque offset index 60B2_h is a common object data index in CiA402, which means that the proposed dynamic feedforward strategy can be applied in many other servo systems based on EtherCAT communication.

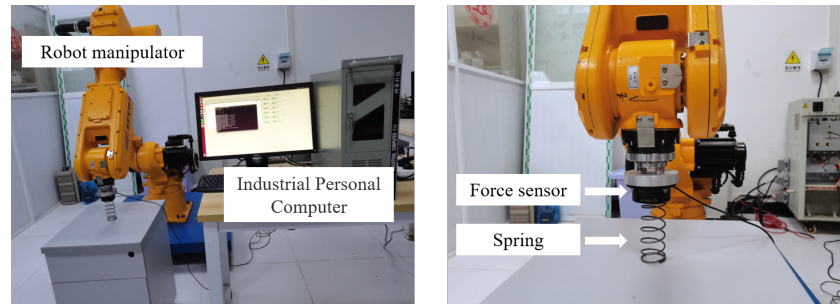


Figure 14. Experimental setup.

Table 6. Experimental setup description and parameters.

Items	Brand and Model	Description
Robot manipulator	EFORT ERC20C-C10	Degree-of-freedom: 6; Maximum load: 20 Kg;
Industrial computer	ADVANTECH	Main board: advantech AIMB-785; Processor: Intel Core™ i7-7700/ 3.6 GHz;
Servo drive	TSINO DYNATRON CoolDrive R6	Maximum EtherCAT communication frequency: 4 KHz;
Force sensor	HPS-FT060E	Range in Z-axis: ±1000 N; Measurement accuracy: 0.4 N; Maximum EtherCAT communication frequency: 2 KHz;
Spring		Stiffness: 1293.83 N/m;

Table 7. ERC20-C10 modified DH parameters.

Link	Joint Offset (d) (m)	Link Length (a) (m)	Link Twist (α) (rad)
1	0.504	0.16846	1.5708
2	0	0.78155	0
3	0	0.14034	1.5708
4	0.76039	0	−1.5708
5	0	0	1.5708
6	0.125	0	0

3.2.2. Experimental Tests

To validate the effectiveness of the proposed FOIC and DFF-FOIC, experiments were carried out as described in this section.

(1) FOIC and IOIC comparison

In this section, the design of the FOIC is investigated considering the tracking performance and the anti-disturbance performance.

First, the FOIC was designed mainly considering the tracking performance and compared with the IOIC under the same frequency domain. The FOIC and IOIC were designed and compared under the same frequency-domain specifications for fair comparison of $\omega_c = 30$ rad/s and $\varphi_m = 40^\circ$. The parameters of the IOIC were designed according to Equations (13) and (14), with $u = 1$, for which the results are $M_d = 1.1013$ kg and

$B_d = 27.7219$ N·s/m. The force step tracking curves are shown in Figure 15. The implemented experiments were repeated ten times. The average performance comparisons are shown in Table 8. The results show that the FOIC has faster response speed, smaller overshoot, and less settling time than IOIC.

The stability of the designed FOIC is proven as follows. Entering the parameters into Equation (18), we choose $u = 1.02$, $\lambda = 1/q = 0.02$, $w = s^\lambda = s^{0.02}$, $q = 50$, and $p = 51$; the pole plot is shown in Figure 16. The slopes of the two stable region boundaries are $\pm\lambda\frac{\pi}{2}$, corresponding to $\pm\frac{\pi}{2}$ for the integer order system. Thus, the system should be BIBO-stable according to the stability analysis in Section 2.3.

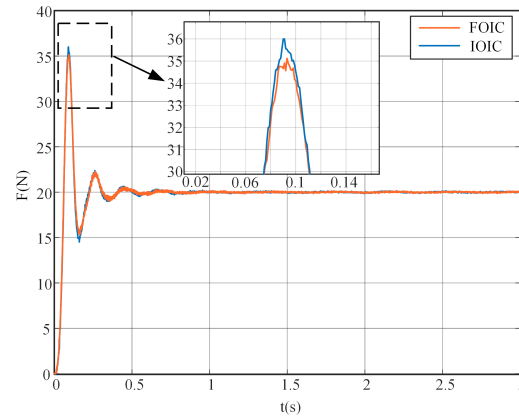


Figure 15. Force step response curve comparison for IOIC and FOIC.

Table 8. Force step response average performance comparison for IOIC and FOIC with ten repetitions.

	IOIC	FOIC	Comparison
Rising time (s)	0.0614	0.0611	0.4886%
Overshoot (N)	76.68%	74.73%	2.54%
Settling time (s)	0.5359	0.4791	10.60%
ITAE	0.3791	0.3478	8.2564%

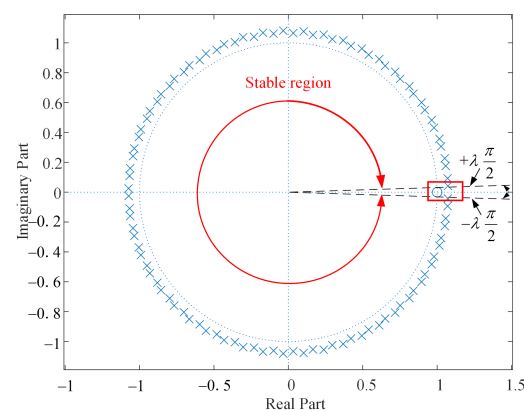


Figure 16. Pole plot of the designed FOIC closed-loop control system.

Second, the FOIC was designed considering anti-disturbance performance and compared with IOIC under the same frequency domain of $\omega_c = 30$ rad/s and phase margin $\varphi_m = 40^\circ$. The design process was as described in Section 2.2; a contact force disturbance of 3 N was added in steady state during the design process of the FOIC. With the influence of force disturbance, the contact force dropped off and then quickly reached steady state at the given reference contact force. The final designed FOIC with the smallest J_{ITSE} was $M_d = 1.0722$ kg and $B_d = 25.9117$ N·s/m, and $u = 1.02$, while the IOIC was

$M_d = 1.1013$ kg and $B_d = 27.7219$ N·s/m. The average performance results for ten repetitions of the anti-disturbance experiment are listed in Table 9. The Bode sensitivity plots for FOIC and IOIC are shown in Figure 17; it can be seen that FOIC has better ability to reject disturbances compared to IOIC.

Table 9. Anti-disturbance response average performance comparison of IOIC and FOIC for ten repetitions.

	IOIC	FOIC	Improvement Comparison of FOIC
Settling time (s)	0.7548	0.7051	6.5845%
ITAE	0.2109	0.2081	1.3276%

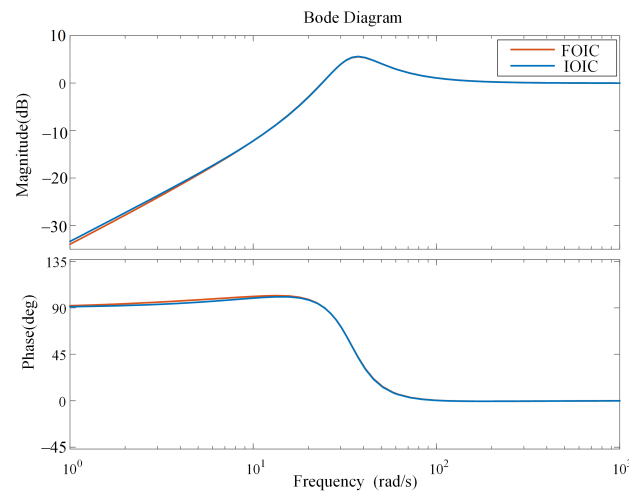


Figure 17. Bode sensitivity plot of FOIC and IOIC for robot manipulator control systems.

The stability of the closed-loop system under the effects of disturbances was addressed by identifying the robot manipulator system of the EFORT ER20C-10, including the inverse kinematics, servos of the joints, and forward kinematics, using the obtained experimental data. The inverse and forward kinematic were described linearly due to the small range of motion in the experiment. The servos of the joints were modeled by first-order systems. The transfer function of the robot manipulator in the impedance control experiment is as follows:

$$G_r(s) = \frac{a_1s + a_0}{b_2s^2 + b_1s + b_0}, \quad (40)$$

where $a_1 = 5170.733366$, $a_0 = 7.779515177 \times 10^6$, $b_2 = 1$, $b_1 = 7223.609339$, and $b_0 = 7.790596290 \times 10^6$.

See Appendix A for the detailed identification.

The closed-loop transfer function of FOIC considering the robot manipulator system is

$$\Phi_2(s) = \frac{(a_1s + a_0)K_s}{M_d b_2 s^4 + B_d b_2 s^{u+2} + M_d b_1 s^3 + B_d b_1 s^{u+1} + M_d b_0 s^2 + B_d b_0 s^u + K_s a_1 s + K_s a_0}. \quad (41)$$

The stability of the designed FOIC robot manipulator is proven as follows. Entering the parameters into Equation (26), we choose $u = 1.02$, $\lambda = 1/q = 0.02$, $w = s^\lambda = s^{0.02}$, $q = 50$, and $p = 51$; the pole plot is shown in Figure 18. The slopes of the two stable region boundaries for the integer order system are $\pm \lambda \frac{\pi}{2}$. The minimum argument of the root is 0.0391 rad, and the argument of the stability bound is 0.0314 rad; thus, the system should be BIBO stable.

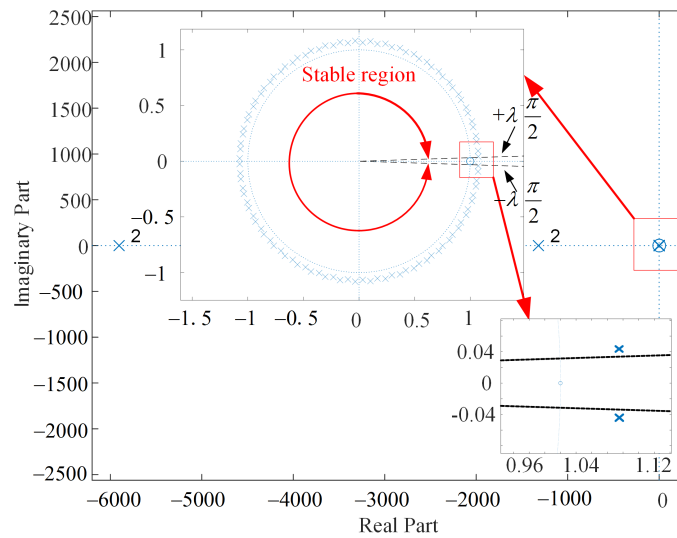


Figure 18. Pole plot of the designed FOIC closed-loop control system considering the robot manipulator system.

(2) FOIC and DFF-FOIC comparison

Although FOIC achieved better control performance than IOIC, FOIC can be further improved by DFF-FOIC.

The dynamic feedforward method was verified to improve the performance of FOIC with $M_d = 1.0722$ kg, $B_d = 25.9117$ N·s/m, and $u = 1.02$. The robot manipulator is severely affected by dynamic disturbances during motion. The step force tracking results are shown in Figure 19, and the experimental performance indexes are listed in Table 10. These results demonstrate that the robot with dynamic feedforward can effectively suppress dynamic disturbances and improve the performance of FOIC.

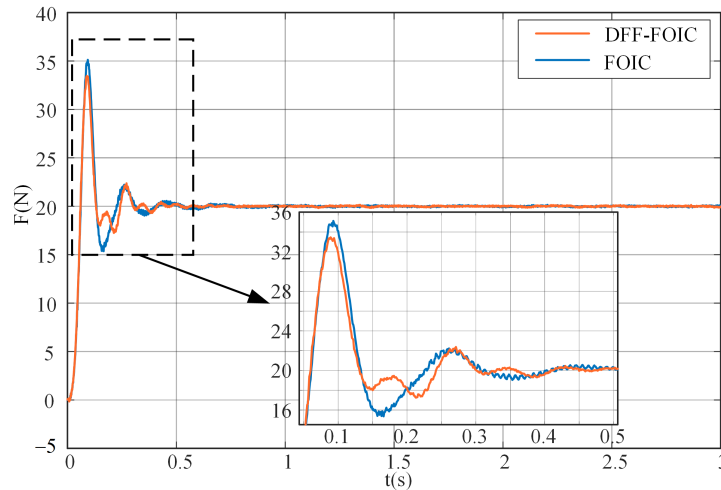


Figure 19. Force step response curve comparison for FOIC and DFF-FOIC.

Table 10. Force step response performance comparison for FOIC and DFF-FOIC.

	FOIC	DFF-FOIC	Comparison
Rising time (s)	0.061	0.06	16.39%
Overshoot (N)	75.62%	67.33%	10.96%
Settling time (s)	0.474	0.431	9.07%
ITAE	0.3619	0.317	12.41%

With dynamic feedforward, the rising time is improved by 16.39%, the overshoot is reduced by 10.96%, and the settling time is reduced by 9.07%. In addition, DFF-FOIC has better ITAE than FOIC by 12.41%. The tracking performance of the servo systems is improved, as shown in Figure 20. As for $Joint_2$ and $Joint_3$, ITAE is improved by 44.44% and 37.5%, respectively, as shown in Table 11.

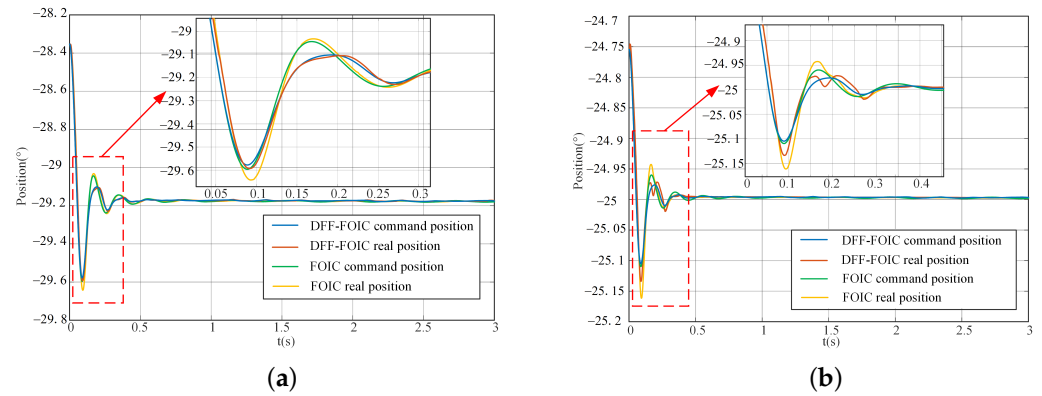


Figure 20. Joint-tracking curve comparison of FOIC and DFF-FOIC. (a) $joint_2$. (b) $joint_3$.

Table 11. ITAE joint-tracking comparison of FOIC and DFF-FOIC.

	FOIC	DFF-FOIC	Comparison
$Joint_2$	0.0099	0.0055	44.44 %
$Joint_3$	0.004	0.0025	37.5 %

(3) DFF-FOIC robustness study

The robustness of the robot manipulator system from (2) above was examined under DFF-FOIC. Different contact force disturbances were added to the system by setting a virtual force disturbance parameter in the control system, with $F_{dis} = 0$ N, $F_{dis} = 2$ N, $F_{dis} = 4$ N, and $F_{dis} = 6$ N. The results show that the proposed DFF-FOIC can maintain a stable state even under influence from force disturbances, and can achieve the desired robustness performance, as shown in Figure 21.

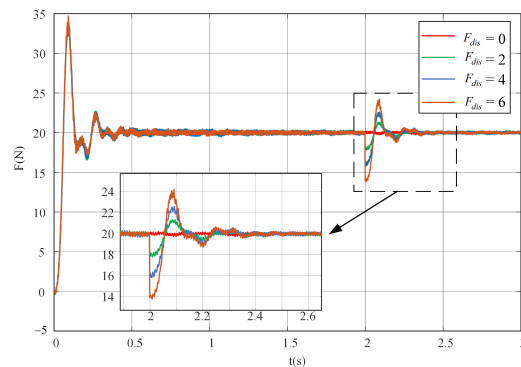


Figure 21. Robustness examination for DFF-FOIC.

(4) Performance comparison with NSGA-IC

In this part, the proposed controller is compared with a state-of-art impedance control scheme, the non-dominated sorting genetic algorithm II-based impedance controller (NSGA-IC) [34]. The integer order impedance control parameters of NSGA-IC are designed by a multi-objective genetic algorithm NSGA-II. In this part, a comparison between the proposed FOIC and the NSGA-IC is carried out. In order to further illustrate the

effectiveness of the dynamic feedforward method, DFF-FOIC is compared with dynamic feedforward-based NSGA-IC (DFF-NSGA-IC).

First, the NSGA-IC is designed as follows. The impedance model is as shown in Equation (3). The rise time (T_r), total variation (T_v), and steady state error (E_{ss}) are chosen as the optimization metrics, with K_d set as 0 to eliminate the steady state error. The optimization problem is presented in Equation (42):

$$\begin{aligned} \min_x \quad & (T_v, T_r, E_{ss}) \\ & X = [M_d, B_d]^T \\ \text{s.t.} \quad & 0 \leq M_d \leq 100 \text{ Kg} \\ & 0 \leq B_d \leq 100 \text{ N} \cdot \text{s/m} \end{aligned} \quad (42)$$

Generations and individuals in NSGA-IC were set as 20 and 20, respectively. The designed parameters of NSGA-IC are $M_d = 2.9871$ kg and $B_d = 25.2114$ N·s/m.

The frequency-domain specifications of the optimized NSGA-IC are gain crossover $\omega_c = 20$ rad/s and phase margin $\varphi_m = 22.9^\circ$. In order to compare the performance of FOIC and NSGA-IC fairly, the FOIC was designed with the same frequency specifications as NSGA-IC, that is, $M_d = 0.7730$ kg, $B_d = 6.8271$ N·s/m, and $u = 1.67$. The results show that the proposed FOIC achieves better response speed, a lower settling time, and better ITSE than NSGA-IC. In order to illustrate the performance of the dynamic feedforward method, dynamic feedforward-based NSGA-IC(DFF-NSGA-IC) was implemented. The experimental results show that DFF-NSGA-IC has better control performance than NSGA-IC, which verifies the performance of the dynamic feedforward method. DFF-FOIC can achieve better response performance and robustness performance than DFF-NSGA-IC. Furthermore, the controller design process of NSGA-IC takes a much longer time than the method proposed in this paper for tuning the parameters of FOIC. The comparisons are shown in Figure 22 and Table 12.

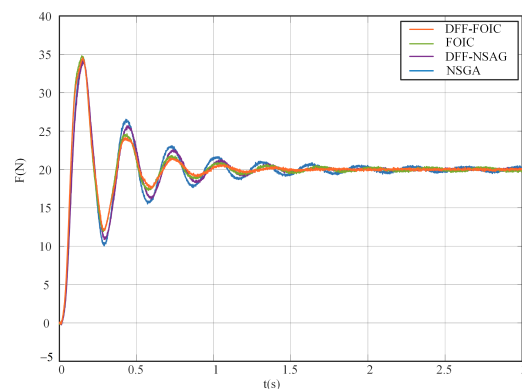


Figure 22. Performance comparison of FOIC, DFF-FOIC, NSGA-IC and DFF-NSGA-IC.

Table 12. Force step response performance comparison of FOIC, DFF-FOIC, NSGA-IC, and DFF-NSGA-IC.

	NSGA-IC	FOIC	DFF-NSAG	DFF-FOIC
Rising time (s)	0.083	0.074	0.083	0.074
Overshoot (N%)	72.09%	74.03%	70.94%	72.87%
Settling time (s)	1.311	0.910	1.204	0.781
ITAE	2.751	1.813	2.599	1.260

4. Conclusions

In this paper, an FOIC is proposed to achieve better contact force control performance of robot manipulators than IOIC. A systematic parameter tuning method is presented

based on frequency-domain specifications. The impact of dynamic disturbances on robot manipulators is investigated. DFF-FOIC is proposed to further improve the performance of FOIC in high-speed response working scenes. The effectiveness of the proposed DFF-FOIC is verified via both simulations and experiments. Our results show that DFF-FOIC can effectively suppress dynamic disturbance impacts in a robot manipulator and achieve the desired control performance.

Author Contributions: Conceptualization, Y.L.; Methodology, Y.D. and Y.L.; Investigation, Y.D.; Data curation, Y.D.; Writing—original draft, Y.D.; Writing—review & editing, Y.L. and Y.C. All authors have read and agreed to the published version of the manuscript.

Funding: This work was supported by the National Natural Science Foundation of China [51975234].

Data Availability Statement: Not applicable.

Conflicts of Interest: The authors declare no conflict of interest.

Appendix A. Identification of Robot Manipulator System

The model of the robot manipulator system shown in Figure 7 is identified according to the collected experimental data of FOIC with $\omega_c = 30$ rad/s and $\varphi_m = 40^\circ$, including the inverse kinematic, servos of joints, and forward kinematics. The inverse kinematics process is used to obtain the desired joint position according to the robot end command in Cartesian space. The forward kinematics process is used to calculate the position of the robot end in Cartesian space according to the joint positions.

In the FOIC experiment for the EFORT ER20C-10, only the contact force in the Z axis in the Cartesian space is moved, with a motion of 2 cm; $joint_2$, $joint_3$, and $joint_5$ are used with only a small motion range. Thus, the relationship between the command in the Z axis in Cartesian space and the joint position can be linear. The identification results of inverse kinematic are as follows:

$$\begin{aligned}\theta_2(t) &\triangleq ik_2(t) = ik_{2a}Z(t) + ik_{2b}, \\ \theta_3(t) &\triangleq ik_3(t) = ik_{3a}Z(t) + ik_{3b}, \\ \theta_5(t) &\triangleq ik_5(t) = ik_{5a}Z(t) + ik_{5b}.\end{aligned}\tag{A1}$$

where $Z(t)$ is a command in the Z axis in Cartesian space, $\theta_i(t)$ ($i = 1, 2, \dots, 6$) is the joint position, $ik_{2a} = 8.955 \times 10^{-4}$, $ik_{2b} = 0.5896$, $ik_{3a} = 2.8210 \times 10^{-4}$, $ik_{3b} = -0.5850$, $ik_{5a} = -0.0012$, and $ik_{5b} = -0.0118$.

The model of the servos is described by the first-order system. The identified results are as follows:

$$\begin{aligned}Q_2(s) &= \frac{1}{1.694 \times 10^{-4}s + 0.9999}, \\ Q_3(s) &= \frac{1}{7.5819 \times 10^{-4}s + 1.0000}, \\ Q_5(s) &= \frac{1}{1.6746 \times 10^{-4}s + 1.0000}.\end{aligned}\tag{A2}$$

where $Q_i(s)$ ($i = 2, 3, 5$) is the transfer function of servo of $joint_i$.

The model of the forward kinematics is linear within the defined motion range. The expression of the forward kinematics of the EFORT ERC20C-10 is as follows, with $\theta_1 = 0$ rad, $\theta_4 = 0$ rad, and $\theta_6 = 0$ rad:

$$\begin{aligned}Z(t) &= d_1 - d_6 \cos(\theta_2(t) + \theta_3(t) + \theta_5(t)) - d_4 \cos(\theta_2(t) + \theta_3(t)) \\ &\quad + a_3 \sin(\theta_2(t) + \theta_3(t)) + a_2 \sin(\theta_2(t)),\end{aligned}\tag{A3}$$

where $Z(t)$ is a command in the Z axis in Cartesian space, d_1, d_4, d_6, a_2, a_3 are the DH parameters for ERC20-C10 as seen in Table 7, and $\theta_i(t)$ ($i = 1, 2, \dots, 6$) is the joint position. The nonlinear items $\sin(\theta_2(t))$, $\cos(\theta_2(t) + \theta_3(t))$, $\sin(\theta_2(t) + \theta_3(t))$, and $\cos(\theta_2(t) + \theta_3(t) +$

$\theta_5(t)$ can be described linearly due to the small motion range of $\theta_i(t)$ ($i = 1, 2, \dots, 6$). The identified results are as follows:

$$\begin{aligned} \sin(\theta_2(t)) &\triangleq s_2(t) = s_{2a}\theta_2(t) + s_{2b}, \\ \sin(\theta_2(t) + \theta_3(t)) &\triangleq s_{23}(t) = s_{23a}(\theta_2(t) + \theta_3(t)) + s_{23b}, \\ \cos(\theta_2(t) + \theta_3(t)) &\triangleq c_{23}(t) = c_{23a}(\theta_2(t) + \theta_3(t)) + c_{23b}, \\ \cos(\theta_2(t) + \theta_3(t) + \theta_5(t)) &\triangleq c_{235}(t) = c_{235a}(\theta_2(t) + \theta_3(t) + \theta_5(t)) + c_{235b}. \end{aligned} \quad (A4)$$

where $s_{2a} = 0.4842$, $s_{2b} = 0.3591$, $s_{23a} = 0.8081$, $s_{23b} = 0.0800$, $c_{23a} = -0.5890$, $c_{23b} = 1.1791$, $c_{235a} = 0.000$, and $c_{235b} = 1$.

The identified robot manipulator system structure is shown in Figure A1.

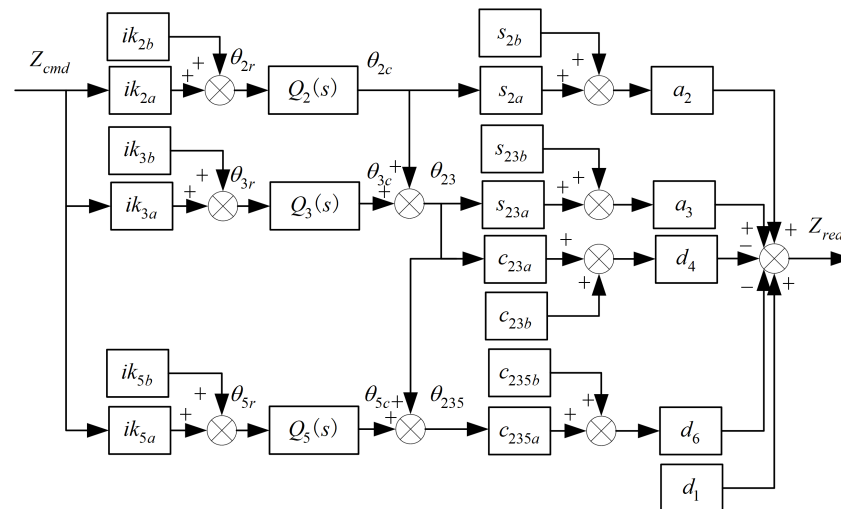


Figure A1. The structure of the identified robot manipulator system.

where θ_{ir} and θ_{ic} ($i = 2, 3, 5$) are the desired and the real positions of $joint_i$, respectively, θ_{23} is the sum position of θ_2 and θ_3 , and θ_{235} is the sum position of θ_2 , θ_3 , and θ_5 .

According to the above results, the derived transfer function of the robot manipulator system in the impedance control experiment is as follows:

$$G_r(s) = \frac{a_1s + a_0}{b_2s^2 + b_1s + b_0} \quad (A5)$$

where $a_1 = 5170.733366$, $a_0 = 7.779515177 \times 10^6$, $b_2 = 1$, $b_1 = 7223.609339$, and $b_0 = 7.790596290 \times 10^6$.

References

- Xu, J.; Zhang, C.; Liu, Z.; Pei, Y. A review on significant technologies related to the robot-guided intelligent bolt assembly under complex or uncertain working conditions. *IEEE Access* **2019**, *7*, 136752–136776. [CrossRef]
- Zhang, B.; Wu, J.; Wang, L.; Yu, Z. Accurate dynamic modeling and control parameters design of an industrial hybrid spray-painting robot. *Robot. Comput.-Integr. Manuf.* **2020**, *63*, 101923. [CrossRef]
- He, Y.; Mei, J.; Fang, Z.; Zhang, F.; Zhao, Y. Minimum energy trajectory optimization for driving systems of palletizing robot joints. *Math. Probl. Eng.* **2018**, *2018*, 7247093. [CrossRef]
- Zhu, D.; Feng, X.; Xu, X.; Yang, Z.; Li, W.; Yan, S.; Ding, H. Robotic grinding of complex components: A step towards efficient and intelligent machining—challenges, solutions, and applications. *Robot. Comput.-Integr. Manuf.* **2020**, *65*, 101908. [CrossRef]
- Yang, C.; Xie, Y.; Liu, S.; Sun, D. Force modeling, identification, and feedback control of robot-assisted needle insertion: A survey of the literature. *Sensors* **2018**, *18*, 561. [CrossRef] [PubMed]
- Zeng, G.; Hemami, A. An overview of robot force control. *Robotica* **1997**, *15*, 473–482. [CrossRef]
- Hogan, N. Impedance Control: An Approach to Manipulation: Part II—Implementation. *J. Dyn. Syst. Meas. Control* **1985**, *107*, 8–16. [CrossRef]

8. Al-Shuka, H.F.; Leonhardt, S.; Zhu, W.H.; Song, R.; Ding, C.; Li, Y. Active impedance control of bioinspired motion robotic manipulators: An overview. *Appl. Bionics Biomech.* **2018**, *2018*, 8203054. [[CrossRef](#)] [[PubMed](#)]
9. Hogan, N. Impedance control: An approach to manipulation. In Proceedings of the 1984 American Control Conference, San Diego, CA, USA, 6–8 June 1984; pp. 304–313.
10. Schmidt, A.; Gaul, L. On a critique of a numerical scheme for the calculation of fractionally damped dynamical systems. *Mech. Res. Commun.* **2006**, *33*, 99–107. [[CrossRef](#)]
11. Kobayashi, Y.; Onishi, A.; Hoshi, T.; Kawamura, K.; Hashizume, M.; Fujie, M.G. Validation of viscoelastic and nonlinear liver model for needle insertion from in vivo experiments. In Proceedings of the International Workshop on Medical Imaging and Virtual Reality, Tokyo, Japan, 1–2 August 2008; pp. 50–59.
12. Sun, H.; Zhang, Y.; Baleanu, D.; Chen, W.; Chen, Y. A new collection of real world applications of fractional calculus in science and engineering. *Commun. Nonlinear Sci. Numer. Simul.* **2018**, *64*, 213–231. [[CrossRef](#)]
13. Niu, H.; Chen, Y.; West, B.J. Why do big data and machine learning entail the fractional dynamics? *Entropy* **2021**, *23*, 297. [[CrossRef](#)]
14. Chen, P.; Luo, Y. A Two-Degree-of-Freedom Controller Design Satisfying Separation Principle With Fractional-Order PD and Generalized ESO. *IEEE/ASME Trans. Mechatronics* **2021**, *27*, 137–148. [[CrossRef](#)]
15. Luo, Y.; Zhang, T.; Lee, B.; Kang, C.; Chen, Y. Fractional-order proportional derivative controller synthesis and implementation for hard-disk-drive servo system. *IEEE Trans. Control Syst. Technol.* **2013**, *22*, 281–289. [[CrossRef](#)]
16. Dadkhah Khiabani, E.; Ghaffarzadeh, H.; Shiri, B.; Katebi, J. Spline collocation methods for seismic analysis of multiple degree of freedom systems with visco-elastic dampers using fractional models. *J. Vib. Control* **2020**, *26*, 1445–1462. [[CrossRef](#)]
17. Agila, A.; Baleanu, D.; Eid, R.; Irfanoglu, B. A freely damped oscillating fractional dynamic system modeled by fractional Euler–Lagrange equations. *J. Vib. Control* **2018**, *24*, 1228–1238. [[CrossRef](#)]
18. Yang, C.; Jiang, Y.; He, W.; Na, J.; Li, Z.; Xu, B. Adaptive parameter estimation and control design for robot manipulators with finite-time convergence. *IEEE Trans. Ind. Electron.* **2018**, *65*, 8112–8123. [[CrossRef](#)]
19. Zhang, B.; Wu, J.; Wang, L.; Yu, Z.; Fu, P. A method to realize accurate dynamic feedforward control of a spray-painting robot for airplane wings. *IEEE/ASME Trans. Mechatronics* **2018**, *23*, 1182–1192. [[CrossRef](#)]
20. Hui, J.; Pan, M.; Zhao, R.; Luo, L.; Wu, L. The closed-form motion equation of redundant actuation parallel robot with joint friction: An application of the Udwardia–Kalaba approach. *Nonlinear Dyn.* **2018**, *93*, 689–703. [[CrossRef](#)]
21. Yao, J.; Deng, W.; Jiao, Z. Adaptive control of hydraulic actuators with LuGre model-based friction compensation. *IEEE Trans. Ind. Electron.* **2015**, *62*, 6469–6477. [[CrossRef](#)]
22. Wu, J.; Li, W.; Xiong, Z. Identification of robot dynamic model and joint frictions using a baseplate force sensor. *Sci. China Technol. Sci.* **2022**, *65*, 30–40. [[CrossRef](#)]
23. Xie, Z.; Xie, F.; Liu, X.J.; Wang, J.; Mei, B. Tracking error prediction informed motion control of a parallel machine tool for high-performance machining. *Int. J. Mach. Tools Manuf.* **2021**, *164*, 103714. [[CrossRef](#)]
24. Liu, L.; Tian, S.; Xue, D.; Zhang, T.; Chen, Y. Industrial feedforward control technology: A review. *J. Intell. Manuf.* **2019**, *30*, 2819–2833. [[CrossRef](#)]
25. Wu, J.; Wang, J.; You, Z. An overview of dynamic parameter identification of robots. *Robot. Comput.-Integr. Manuf.* **2010**, *26*, 414–419. [[CrossRef](#)]
26. Huo, W. New formulas for complete determining base parameters of robots. In Proceedings of the 1995 IEEE International Conference on Robotics and Automation, Nagoya, Japan, 21–27 May 1995; Volume 3, pp. 3021–3026.
27. Swevers, J.; Ganseman, C.; Tukul, D.B.; De Schutter, J.; Van Brussel, H. Optimal robot excitation and identification. *IEEE Trans. Robot. Autom.* **1997**, *13*, 730–740. [[CrossRef](#)]
28. Swevers, J.; Ganseman, C.; De Schutter, J.; Van Brussel, H. Experimental robot identification using optimised periodic trajectories. *Mech. Syst. Signal Process.* **1996**, *10*, 561–577. [[CrossRef](#)]
29. Caputo, M. Mean fractional-order-derivatives differential equations and filters. *Ann. dell'Univ. Ferrara* **1995**, *41*, 73–84. [[CrossRef](#)]
30. Jung, S.; Hsia, T.C. Stability and convergence analysis of robust adaptive force tracking impedance control of robot manipulators. In Proceedings of the 1999 IEEE/RSJ International Conference on Intelligent Robots and Systems. Human and Environment Friendly Robots with High Intelligence and Emotional Quotients, Kyongju, Korea, 17–21 October 1999; Volume 2, pp. 635–640.
31. Lee, K.; Buss, M. Force tracking impedance control with variable target stiffness. *IFAC Proc. Vol.* **2008**, *41*, 6751–6756. [[CrossRef](#)]
32. Kim, T.; Kim, H.S.; Kim, J. Position-based impedance control for force tracking of a wall-cleaning unit. *Int. J. Precis. Eng. Manuf.* **2016**, *17*, 323–329. [[CrossRef](#)]
33. Chen, G.; Guo, S.; Hou, B.; Wang, J.; Wang, X. Fractional order impedance control. In *Nonlinear Dynamics and Control*; Springer: Cham, Switzerland, 2020; pp. 167–175.
34. Lahr, G.J.; Garcia, H.B.; Savazzi, J.O.; Moretti, C.B.; Aroca, R.V.; Pedro, L.M.; Barbosa, G.F.; Caurin, G.A. Adjustable interaction control using genetic algorithm for enhanced coupled dynamics in tool-part contact. In Proceedings of the 2017 IEEE/RSJ International Conference on Intelligent Robots and Systems (IROS), Vancouver, BC, Canada, 24–28 September 2017; pp. 1630–1635.
35. Matignon, D. Stability results for fractional differential equations with applications to control processing. *Comput. Eng. Syst. Appl.* **1996**, *2*, 963–968.

36. Atkeson, C.G.; An, C.H.; Hollerbach, J.M. Estimation of inertial parameters of manipulator loads and links. *Int. J. Robot. Res.* **1986**, *5*, 101–119. [[CrossRef](#)]
37. Impulse Response Invariant Discretization of Fractional Order Integrators/Differentiators. Available online: <http://www.mathworks.com/matlabcentral/fileexchange/21342-impulse-response-invariant-discretization-of-fractional-order-integrators-differentiators> (accessed on 1 September 2020).

Disclaimer/Publisher's Note: The statements, opinions and data contained in all publications are solely those of the individual author(s) and contributor(s) and not of MDPI and/or the editor(s). MDPI and/or the editor(s) disclaim responsibility for any injury to people or property resulting from any ideas, methods, instructions or products referred to in the content.